Soft Matter

Anisotropy effects on the kinetics of colloidal crystallization and melting: comparison of spheres and ellipsoids

Journal:	*Soft Matter*
Manuscript ID	SM-ART-05-2019-000887.R1
Article Type:	Paper
Date Submitted by the Author:	15-Aug-2019
Complete List of Authors:	Kao, Peng-Kai; University of Michigan, Chemical Engineering VanSaders, Bryan; University of Michigan, Materials Science & Engineering Durkin, Michael; University of Michigan, Chemical Engineering Glotzer, Sharon; University of Michigan, Chemical Engineering Solomon, Michael; University of Michigan, Chemical Engineering

SCHOLARONE™
Manuscripts

Anisotropy Effects on The Kinetics of Colloidal Crystallization and Melting: Comparison of Spheres and Ellipsoids

Peng-Kai Kao[a], Bryan J. VanSaders[b], Michael D. Durkin[a], Sharon C. Glotzer[a,b] and Michael J. Solomon[a]
[a]Department of Chemical Engineering, University of Michigan, Ann Arbor, Michigan
[b]Department of Materials Science & Engineering, University of Michigan, Ann Arbor, Michigan

Corresponding Author
Prof. Michael J. Solomon
Address: North Campus Research Complex, Building 10 – A151, 2800 Plymouth Road, Ann Arbor, MI 48109
Phone: 734 -764-3119
Email: mjsolo@umich.edu

Abstract

We use alternating current (AC) electric field assisted self-assembly to produce two-dimensional, millimeter scale arrays of ellipsoidal colloids and study the kinetics of their phase reconfiguration by means of confocal microscopy, light scattering, and computer simulation. We find that the kinetics of orientational and positional ordering can be manipulated by changing the shape of the colloids: ellipsoids with aspect ratio 2.0 melt into disordered structures 5.7 times faster compared to spheres. On the other hand, ellipsoids self-assemble into ordered crystals at a similar rate to spheres. Confocal microscopy is used to directly visualize defects in the self-assembled structures. Small-angle light scattering (SALS) quantifies the light diffraction response, which is sensitive to the kinetics of positional and orientational ordering in the self-assembled anisotropic structures. We find three different light diffraction patterns: a phase with high orientational order (with chain-like structure in real space), a phase with high positional and orientational order (characteristic of a close-packed structure), and a phase that is disordered in position but with intermediate orientational order. The large influence of aspect ratio on the kinetics of the positionally and orientationally ordered phase is explored through simulation; it is found that the number of particle degrees of freedom controls the difference between the melting rates of the ellipsoids and spheres. This research contributes to the understanding of reconfiguration kinetics and optical properties of colloidal crystals produced from anisotropic colloids.

1. Introduction

Self-assembled colloids can reconfigure their equilibrium phase or lattice parameter through dynamic manipulation of physical parameters such as the colloid size, shape, and interaction potential as well as the magnitude and direction of externally applied fields.[1] Photo-induced[2], electrophoretic, electrokinetic[3–8], and acoustic assembly[9] have been used to drive reconfigurable colloidal assembly. Applications of such kinetic information include the development of reconfigurable structural color[10] as well as soft robotics[11] and sensing[12]. In addition, some animals – including chameleons[13] and cephalopods[14] – are able to rapidly switch their coloration through reconfiguration of iridophores, which are structures that use diffraction to produce biological coloration[15–17]. In artificial systems, self-assembled colloids that can reconfigure their phase or lattice parameter offer similar possibilities for active coloration. Control of temperature[18], osmotic pressure[19] and the strength of electric fields[20] have been demonstrated to shift the wavelength of Bragg iridescence; however, more information about the kinetics of phase changes in such driven systems is needed.

Applications in which optical response is controlled by reconfiguration of ordered colloidal structures can be facilitated by better understanding what factors control the kinetics of crystallization and melting, which are the physical processes that control reconfiguration. Here we perform a comparative study of such in suspensions of colloidal spheres and ellipsoids. The kinetics of crystallization and melting has received significant attention in colloid science.[21–23] In this article, we extend the study of colloidal phase transitions to compare such transitions in systems spheres and ellipsoids, as driven by the application of an electric field. The comparison of isotropic and anisotropic shapes[24,25] illuminates the fundamental effect of building block anisotropy on the kinetics of field-induced phase change, as observed by light diffraction. Comparing the simple geometries of spheres and ellipsoids is an ideal way to study the role of anisotropy in determining local and global order.

Confocal laser scanning microscopy (CLSM) is used to visualize the particle-level microstructure, including crystal arrays with vacancies, dislocations, and grain boundaries. We characterize the local microstructure of three different kinds of colloidal assemblies (chains, close-packed

structures, and dense positionally disordered structures) using CLSM. Positional and orientational order parameters are used to describe the short-range defect types and density observed by CLSM. Small-angle light scattering (SALS)[26,27] is used to characterize global, ensemble-averaged colloidal crystal quality through measurement of the integrated intensity of light diffraction peaks. This measure includes information about the intensity and azimuthal angular broadening of diffraction peaks; it can thus be used as a measure of the quality of global order. We use these measures to investigate the kinetics of crystal quality development by executing a reconfigurable fluid-crystal transition with AC electric fields. A molecular dynamics simulation model is developed to explore how polarization-induced forces, as generated by AC electric fields, drive assembly, and how particle geometry affects the kinetics of crystal assembly and melting. Using a coarse-grained representation of polarization-induced forces and excluded volume interactions only, the simulations demonstrate a large difference in melting kinetics between isotropic and anisotropic particles. From simulations, we find that this difference is linked to rotational dynamics. This result highlights the fundamental effect of building block anisotropy on melting kinetics.

2. Methods and Materials

2.1 Monodisperse Colloidal Ellipsoids

The ellipsoidal particles were produced by uniaxial stretching of polystyrene spheres with diameter 4.00 ± 0.04 μm (F8858, Invitrogen), as described in Shah *et al*.[28] The ellipsoids used in this study have an aspect ratio of 2.0 ± 0.3 (major axis L = 6.4 ± 0.5 μm, minor axis D = 3.2 ± 0.2 μm, as determined by measuring 68 ellipsoids using scanning electron microscopy). After stretching, the ellipsoids were dispersed in 0.1 mM NaCl aqueous solution for self-assembly experiments. Initial colloidal volume fractions of 0.0015, 0.003, and 0.006 were studied. Concentrations were determined by using a hemocytometer (NanoEnTek Inc.). The initial number of colloids per unit surface area of the above systems are 0.044, 0.087 and 0.175 ellipsoids/μm^2, respectively.[29]

2.2 Self-assembly by AC Electric Fields

To generate 2D monolayers of colloids by self-assembly, a coplanar AC electric field device was used. Briefly, the device was prepared by deposition of Au/Ti electrodes onto a glass substrate, as described in Shah *et al*.[11] The device was cleaned before each use by means of a freshly prepared base bath (1N potassium hydroxide solution in ethanol, Fisher Scientific). The colloidal suspension was injected into the device, which is 1 mm in height. It took about one hour for particles to complete the sedimentation process. Particle sedimentation was completed before applying the AC electric field. A square wave with constant root-mean-square voltage (V_{rms}) ranging from 0.5 to 10.0 V and frequencies ranging from 500 Hz to 5 MHz was applied across the 250 μm gap between electrodes by means of an AC power source (RIGOL, DG1022). Particles are more concentrated at the centerline between two electrodes due to dielectrophoresis. The subsequently reported area fraction of particles is computed for the same region in which the relaxation kinetics is studied and characterized. The resulting self-assembled structures were visualized by CLSM (Nikon A1 Piezo z-drive, 100×, NA = 1.45 oil immersion objective). The image size is 512 x 512 square pixels. The pixel size is 250 x 250 nm^2. For kinetics measurements, the frame acquisition rate was 15 frames per second.

2.3 Nearest Neighbors and Nearest Neighbor Angles

We used the number of nearest neighbors and the angles between those neighbors as local order parameters to quantify short-range positional order. The nearest neighbors of each ellipsoidal

particle are identified in the assembled structure by comparing the distance between it and other particles to a chosen cutoff distance set by the radius of an elliptical coordination shell. The major axis of this shell is set as 2.1 times the second peak of g(r) of the close-packed colloidal ellipsoid structure. This cutoff is set to ensure that we include the first coordination shell in the counting. Supplementary Figure S1 (a)-(c) illustrates the process to find the nearest neighbors of a close-packed assembly of ellipsoids. The nearest neighbor angle, θ_{nn}, is also used to determine the quality of local positional ordering of an assembly. As shown in Supplementary Figure S1(a), vectors connecting the centroid of a given particle to the centroids of its nearest neighbors are used to compute a set of nearest neighbor angles.

To quantify the orientational order of each assembled structure, we calculated the 2D alignment factor, $S = \frac{1}{2}\langle 3\langle u_i \cdot u_{ref}\rangle^2 - 1\rangle$.[30,31] The alignment factor has been utilized to quantify the degree of particle orientation in liquid crystalline polymers[32] and ellipsoidal colloidal suspensions.[33] For S = 1, particles are perfectly oriented; S = 0 represents randomly distributed particle orientations.

2.4 Small-Angle Light Scattering (SALS)

The design of the SALS device was adapted from Somwangthanaroj *et al*.[34] (See Supplementary Figure S2). A laser (JDS Uniphase, 1135P) of wavelength 632.8 nm with a $1/e^2$ diameter of 0.71 mm was used. A neutral density filter of optical density 2.0 was used to attenuate the laser light. Two 45-degree mirrors were used to control the path of the light so that the colloidal sample could be placed in the horizontal position. After the laser light was scattered as it traversed the sample, an aspheric lens (diameter = 50 mm, focal length = 37 mm; Newport Inc., Irvine, CA) was used to collimate the scattered light. A pair of achromatic lenses (first achromatic lens, diameter = 50.8 mm, focal length = 250 mm; second achromatic lens, diameter = 12.7 mm, focal length = 40 mm) was utilized to collect the scattered light onto a 12-bit CCD camera. To enhance sensitivity, a beam stop (neutral density filter of optical density 5.0) was placed between the collimating lenses to block the central (unscattered) laser light. From this collected data, the intensities at each scattered angle can be derived. The range of accessible scattering angles is from 2° to 13°.

2.5 Analysis of Light Diffraction Response

SALS is well suited to studying the collective dynamics of colloid assemblies, as it integrates over large areas. The pattern of light scattering recorded for fluid-like and crystal-like colloidal assemblies was primarily contained within a spherical or elliptical ring (for spheres and ellipsoids, respectively). We analyzed this ring to detect the disorder-to-order transition. The major axis of the ring was aligned in the field direction. The radial width of the analyzed region was set to a fixed value of 31 pixels because the average width of the primary scattering patterns was 31±2 pixels (c.f., SI). The average intensity is computed as a function of an azimuthal angle ψ; this angle is defined relative to the field direction. The analyzed region corresponds to a scattering vector q = 1.69 μm^{-1} in the direction of the field and q = 1.11 μm^{-1} in the perpendicular direction, with a radial width $\Delta q \sim 0.32\ \mu m^{-1}$. Here, the scattering wavevector, $q = \frac{4\pi n}{\lambda}\sin\left(\frac{\theta}{2}\right)$, is equal to the difference between the incident wavevector and the scattered wavevector, where n is the effective refractive index of the sample, λ is the wavelength of incident light and θ is the scattering angle.

We use locally weighted smoothing (LOWESS[35]) to fit the intensity data as a function of azimuthal angle to a Gaussian model after baseline correction. Finally, we computed peak intensity, full width at half maximum (FWHM) and peak area of each scattering peak to quantify the light diffraction response. Greater peak intensity or smaller FWHM both represent higher long-range ordering quality of the self-assembly. Peak area incorporates information about both peak intensity and FWHM of the light diffraction response We find that peak area is sensitive to crystallization or melting, while being relatively insensitive to changes that occur after (or before) the system has transitioned. For this reason, we use peak area to quantify the light diffraction response in what follows, although we confirmed that our conclusions were not impacted by the specific choice among these three measures. A comparison of peak area, peak intensity and FWHM of light diffraction peaks as a measure of the colloidal phase change for simulated systems is included in the Supplementary Information (Figure S5).

2.6 Molecular Dynamics Simulations

Simulations of colloid assembly and melting were carried out with HOOMD-Blue[36,37], using Langevin dynamics simulations. The simulated model approximates experimental forces present on colloidal particles via four components: 1. A pair potential interaction with a steep repulsive core (representing excluded volume) and a weak attractive well (representing mild attraction

between neighbors) in spherical or ellipsoidal coordinates; 2. Electrostatic forces between particles representing the effect of induced dipoles; 3. A torque aligning the particles with the field direction; 4. A gravitational force to induce settling. For details concerning the implementation of these forces, see the Supplementary Information.

The parameters of this particle interaction model were tuned to produce the experimentally observed crystal structures for spheres and ellipsoids of aspect ratio 2. This fitting was most sensitive to the parameters governing the electrostatic interactions of the particles. For ellipsoidal particles, different induced dipole moments can produce the crystal structure experimentally observed for spheres or that observed for ellipsoids. For spheres, the preferred motif of charge-mediated interactions is to form chains. Inter-chain attraction due to charge forces alone was too weak to result in long range 2D crystals. A weak direction-independent attraction (the attractive part of the pair potential) was required for long-range spherical crystallization. Changes to the angular freedom of particles under 'field-on' conditions were not found to have strong consequences for the phase behavior of the model, but instead introduced additional spread into the peaks present in the Fourier domain representation of the crystals. The downward force representing gravity was chosen to match the force experienced by a polystyrene sphere of diameter 4.0 μm immersed in water. We found that the magnitude of this force needed to be sufficiently large to prevent the formation of 3D cluster assemblies but was otherwise unimportant to phase behavior. For the force we used, lifting a particle by its own diameter required $13k_bT$.

The initial simulation domain size was chosen so that the global particle area coverage was 0.5. During simulation, particles aggregate and form dense regions. For spheres, local area coverage (calculated in circular regions 20 times the size of a single particle) after assembly was 0.82±0.11. For ellipsoids, local area coverage (calculated for the same area as spheres) was 0.84±0.13.

3. Results

3.1 Light Diffraction Responses of Ellipsoidal Colloid Assemblies

Depending on the initial concentration as well as the strength and frequency of the electric field, structures with a broad range of orientational and positional order were self-assembled. Figure 1 reports representative CLSM and SALS results at each concentration level (initial volume fraction (ϕ_i) 0.0015, 0.003 and 0.006) at an AC electric field strength and frequency of E = 40 kV/m and 5MHz, respectively. For an initial volume fraction of 0.0015, a phase with high orientational order and numerous positional defects was observed by CLSM (Figure 1 a-I). These positional defects were predominantly vacancies that were formed during sedimentation of the dilute colloidal suspension. This chain-like structure is similar to the structure Singh *et al*.[38] reported. Macroscopically, from SALS, a bright diffraction ring pattern was observed (see Figure 1 d-I).

When we doubled the initial volume fraction to 0.003, a phase with both high positional and orientational ordering was observed by CLSM (Figure 1 a-II). A monolayer of close-packed ellipsoids aligned with the AC electric field direction formed after sedimentation. Under the applied electric field, ellipsoidal colloids aligned their long axes with the field and tended to form zig-zag chain configurations with contacts offset from the tip. A clear six-fold diffraction pattern appeared in the SALS (Figure 1 d-II). The SALS diffraction patterns are anisotropic because of the geometry of the unit cell, which is impacted by the ellipsoidal shape of the colloids.

Upon further increase of the initial volume fraction to 0.006, application of the AC electric field yielded a positionally disordered structure, as shown in Figure 1 a-III. This disordered structure is composed of multiple layers of ellipsoids assembled on top of the coplanar electrode. The intensity of the corresponding diffraction response was low (see Figure 1 d-III).

We calculated the area fraction covered by particles as $d_{2D}=N*S_a/A$ where N is the total number of particles in an image from image analysis, S_a is the area of a single ellipsoid, and A is the image area. The area fraction is 60.3% for the chain-like structure, 82.1% for the close-packed structure and 66.2% for the dense positionally disordered structure. The area fraction for the dense positionally disordered structure is for the bottom layer of the structure.

A non-monotonic relationship between the initial volume fraction and the density of the assembled layers is observed. This non-monotonicity is due to arrested crystallization kinetics at the highest initial densities studied. At lower area concentration, the low number of particles per area on the substrate leads to the low density chain-like structure. At intermediate area concentrations, the density is sufficient to permit the formation of a dense crystalline structure. At high concentrations, dynamics are slow enough to yield kinetic trapping, particularly because of the anisotropic shape of the particles and the presence of multiple layers. This sequence of transitions has been predicted theoretically[39] and observed experimentally[28,40] in three dimensions.

For ellipsoids of initial volume fraction of 0.0015, 0.003 and 0.006, the alignment factor (S) values are 0.88 ± 0.02, 0.93 ± 0.01, and 0.58 ± 0.02 respectively. For the dense positionally disordered phase (ϕ_i = 0.006, d_{2D} = 66.2%), S is relatively low and thus is distinguishable from the other two cases. To further distinguish the chain-like structure and the close-packed structure, we turn to analysis based on the position and orientation of nearest neighbors (c.f. Methods). For the chain-like structure (ϕ_i = 0.0015, d_{2D} = 60.3%, S = 0.88), as shown in Figure 1 b-I, the average number of nearest neighbors is 3.5 with standard deviation of 1.1. There are 23±4 % of nearest neighbor angles (θ_{nn}) ranging from 140° to 180° observed in the distribution of nearest neighbor angles (Figure 1 c-I), indicating chaining of ellipsoids due to the polarization attraction between particles and the appearance of vacancies in the assembly. The report of nearest neighbor angles (θ_{nn}) is shown in Figure 1 b-II.

As shown in Figure 1 b-II, for the close-packed structure (ϕ_i = 0.003, d_{2D} = 82.1%, S=0.93), the average nearest neighbors are 5.5 with a standard deviation of 1.3. There are 53±8 % of particles that have six nearest neighbors and 85±4 % of particles that have a number of nearest neighbors between five to seven, indicating this is a hexagonally close-packed structure, which is consistent with the six-fold symmetry we observed in Figure 1 a-II. The real space and light scattering data are connected by Fourier transform. From the nearest neighbor angle distribution analysis (see Figure 1 c-II), we observed two distinct peaks at 41.3±1.3° and 69.4±1.6°. These two peaks are very close to the Fourier transform results of a simulated hexagonally close-packed particles array, with the same particle aspect ratio as in our experiments. The corresponding modeling results are

41.3±0.1 ° and 69.4±0.1 °. The chaining angle between ellipsoids which are half of θ_{nn} is therefore about 20.7°. Singh et al. reported an average chaining angle between 10° and 15° for ellipsoids with three different aspect ratios (3.0, 4.3, and 7.6) assembled in an AC electric field. Azari et al. reported the contact angle between two adjacent ellipsoids at their minimum energy configuration as a function of particles aspect ratio. Using the two-point charge model, a contact angle of 12° between ellipsoids with aspect ratio two was reported.

Lastly, for the dense positionally disordered structure, the average nearest neighbors are 3.9 with a relatively large standard deviation of 2.2 (Figure 1 b-III). No obvious patterns are found for the distribution of nearest neighboring angles (Figure 1 c-III). Thus, we successfully resolve and differentiate between three different structures: hexagonal chain-like structure, close-packed structure and dense positionally disordered structure by introducing the comparison of alignment factor, nearest neighbors and nearest neighboring angles.

We determined the quality of the self-assembled colloidal crystals from analysis of light scattering images (Figure 1 d I-III) by computing the peak area as a function of the azimuthal angle, ψ (cf. Methods and Materials). We assigned the peak at ψ = 20.7°, 90.0°,159.4°, 200.7°, 270.0°, and 339.4° as peak 1, 2, 3, 4, 5, and 6 respectively (Figure 1 d-II). Peaks 2 and 5 are generally much brighter than peaks 1,3,4 and 6 (Figure 1 e I-III). This phenomenon is a consequence of the ellipsoidal shape of the particles; that is, the shape of the scatterer generates the angular variation in the scattering.[41]

For the chain structure, the average peak area of peaks 1,3,4, and 6 is 480±24 arbitrary unit (au) (46% of light scattering peak area compared to that of the close-packed structure), and for peaks 2 and 5 is 985±50 au (21% of light scattering peak area compared to that of the close-packed structure). For the close-packed structure, there are six significant scattering peaks. The average peak area of peaks 1,3,4, and 6 is 1,041±25 au, and the average peak area of peaks 2 and 5 is 4,684±182 au. For the dense positionally disordered structure, the scattering peaks are minimally resolvable with the average peak area of peaks 1,3,4, and 6 equal to 85±14 au (only 8% light scattering peak area compared to that of the close-packed structure), and the peak area of peaks 2 and 5 is 524±38 au (11% light scattering peak area compared to that of the close-packed structure).

The Figure 1 results reveal the connection between the long-range optical properties and the short-range defect microstructures in the ellipsoidal suspensions. The close-packed structure that displays the least number of defects exhibits the most intense light scattering peak area.

3.2 Dependence of Crystal Quality on Self-Assembly Conditions

To study the kinetics of colloidal crystal quality development, we first evaluate the impact of applied electric field strength and applied frequency Ω on ellipsoid self-assembly. We focus on the intermediate initial concentration condition going forward, because this specimen yielded a high-quality single-layer structure with positional and orientational order, as reported in Figure 1. Figure 2 (a) reports images of colloidal self-assembly at electric field strength E= 8 kV/m, 18kV/m and 40kV/m, respectively, with applied frequency fixed at 5MHz, as well as the SALS images of the assembled structures. Prior to application of the electric field, particles are homogeneously dispersed at d_{2D} = 82.1%. For electric field strengths smaller than 8 kV/m, the magnitudes of the light diffraction peak areas are at a minimum level. At E=8 kV/m, the assembled structure is disordered (Figure 2 a-I), and diffraction peaks are minimally resolvable by analysis of light scattering images (Figure 2 a-II). At AC E=18 kV/m, the ellipsoids assemble along the direction of the electric field and form structures with poor crystal quality and abundant local defects (Figure 2 a-III). Peaks 2 and 5 become bright and visible, while peaks 1,3,4, and 6 remain close to background level (Figure 2 a-IV). At E=40 kV/m, close-packed assemblies with a low concentration of defects are observed (Figure 2 a-V). In addition to low defect density in the images, the corresponding SALS image show a bright six-fold diffraction pattern indicative of high global crystal quality (Figure 2 a-VI).

Figure 2 (b) shows the peak area of the light diffraction response (A) under varying electric field strengths with constant applied frequency (5MHz). As the electric field strength was increased, the peak area tended to increase, indicating a field-induced disorder-to-order transition. Once the electric field strength exceeds the threshold value of 24 kV/m, the magnitude of the peak area increased only slowly with field strength. The results demonstrate that good colloidal crystal quality can be achieved as the electric field strength exceeds the threshold value of 24 kV/m.

It is noteworthy that a scattering response at low q is apparent in Figure 2 a-IV and a-VI. This response occurs for $q \leq 0.46\ \mu m^{-1}$. Based on the reciprocity of Fourier transforms, whereby a functional width σ in real-space maps to a spread of $q = 2\pi/\sigma$ in the corresponding diffraction-space, this low q diffraction response is generated from structures of functional width $\sigma \geq 13.7\ \mu m$. This peak is consistent with the device geometry. That is, within the coplanar electric field device which has a gap dimensions of 250 μm, colloidal particles form a dense phase in the center; gradients in particle density are observed along the electric field direction. This real-space phenomenon is consistent with the low-q scattering response.

The frequency of the electric field also influences crystal quality through its effect on the field-induced polarization of the colloids. We measured the crystal quality at various frequencies with a fixed electric field strength of 32kV/m. At frequency $\Omega = 0.5$ kHz, ellipsoidal particles rapidly clustered between the electrodes (Figure 2 c-I). The phenomenon is caused by dielectrophoresis, as observed in other studies.[42] A dim elliptic ring-shape scattering response was observed instead of a six-fold diffraction pattern (Figure 2 c-II). At frequency 100 kHz, colloids assembled into structures with low positional order (Figure 2 c-III), showing elliptical ring-shape scattering (Figure 2 c-IV). Six-fold scattering patterns can be observed as the applied frequency exceeds 0.5 MHz. At frequency 5 MHz, ellipsoidal particles generated colloidal crystals with high positional and orientational order (Figure 2 c-V). The corresponding light scattering image shows a bright six-fold pattern (Figure 2 c-VI).

Figure 2(d) shows the peak area of the light diffraction response with field frequency varying from 0.5 kHz to 5 MHz under constant field strength 32 kV/m. For frequency Ω in the range of 0.5–10 kHz, the magnitudes of light diffraction peak areas are at a minimum level. For 10-100 kHz, the average magnitude of the light diffraction peak areas is 3.6±0.7 times brighter for peaks 2 and 5 and 3.8±0.8 times brighter for peaks 1,3,4 and 6 compared with frequency in the range of 0.5–10 kHz. For Ω in the range of 0.5–5 MHz, the average magnitude of peak areas is 13.4±2.4 times brighter for peaks 2 and 5 and 23.7±2.8 times brighter for peaks 1,3,4 and 6 compared with Ω in the range of 0.5–10 kHz.

The interparticle distance (σ_i) can be calculated from the SALS data based on the reciprocity relationship $q=2\pi/\sigma_i$ between diffraction-space and real-space. From Figure 2(a), the major axis and the minor axis of the SALS pattern are 1.29 μm^{-1} (σ_i = 4.87 μm) and 0.86 μm^{-1} (σ_i = 7.31 μm) at electric field strength 18kV/m. Upon increase of the electric field strength to 40kV/m, the major axis and the minor axis of the SALS pattern are 1.30 μm^{-1} (σ_i = 4.83 μm) and 0.87 μm^{-1} (σ_i = 7.22 μm), respectively. The above results show that interparticle distance decreases with increasing applied field strength. From Figure 2(c), the major axis and the minor axis of the SALS pattern are 1.23 μm^{-1} (σ_i = 5.11 μm) and 0.81μm^{-1} (σ_i = 7.76 μm) for applied frequency 100kHz. With frequency increased to 5MHz, the major axis and the minor axis of the SALS pattern are 1.27 μm^{-1} (σ_i = 4.95 μm) and 0.87 μm^{-1} (σ_i = 7.22 μm). The results also demonstrate that interparticle distance decreases with increasing frequency. These average interparticle distances change only modestly for electric field strength 18-40kV/m and frequency 100kHz-5MHz. However, at the same time the diffraction patterns evolve from a ring (disordered phase) to a six-fold pattern (crystallization). This indicates that while interparticle distances are largely conserved, the particles are aligned in specific directions with increasing electric field strength and frequency.

Based on the above results, we selected E = 32 kV/m and Ω = 5MHz, shown as red boxed data points in Figure 2 (b) and (d), for further kinetic studies. These conditions ensure that the colloidal particles assemble into high quality crystals by means of AC electric fields.

3.3 The Effects of Shape Anisotropy on Colloidal Ordering Kinetics

Figure 3 compares the time-evolution of the SALS peak area of the d_{2D} = 82.1% specimens for the ellipsoids under field-on (assembly) and field-off (melting) conditions. Comparative experiments with spheres were performed at the same conditions. The initial state for the field-on experiments were the disordered suspensions at the initial volume fraction. Particle sedimentation was allowed to complete before the field was switched on; the number of particles within the region probed by SALS does not vary significantly during the study. The melting experiments were conducted by first creating a close-packed crystal with the electric field on for five minutes and then turning off the field. This melting-assembly cycle was repeated five times with 10 minutes between each cycle. The SALS were analyzed as described to obtain the time dependence of the peak area.

Figure 3 (a) shows that there is a monotonic decay of peak area upon melting of the solution of spheres. The six peaks have two sets of decays. It takes approximately 150 seconds for peaks 1,3,4 and 6 to reach the steady-state value and 180 seconds for peaks 2 and 5 to reach the steady-state value. Figure 3 (b) reports the assembly of spheres and shows a monotonic increase of peak area. It takes approximately 70 seconds for all peaks to reach steady-state values.

Under the same experimental conditions, the melting of aspect ratio 2 ellipsoids showed a much faster transition from one peak area to another. As shown in Figure 3(c), it took approximately 30 seconds for peaks 1,3,4, and 6 to reach the steady-state value and 40 seconds for peaks 2 and 5 to reach the steady-state value. The difference in the kinetics between the two sets of peaks may be related to the symmetry breaking of the field. Differences in ordering between the field direction and the other two close-packed directions lead to different melting kinetics. Figure 3(d) reports the assembly of the ellipsoids, showing a monotonic increase of peak area. Similar to the assembly of spheres, it takes the ellipsoids approximately 70 seconds to reach steady-state values of the peak area.

Using a pair potential model appropriate to the conditions of the self-assembly (c.f. Figure 4a and methods), Figure 4 compares the self-assembled structure and diffraction patterns of the experimental and simulated systems. Figure 4 (b) and (d) show CLSM images of spheres and ellipsoids, respectively. These can be compared to Figure 4 (f) and (i) which show the simulated systems. Comparing the SALS diffraction patterns (Figure 4 (c) and (e)) and the 2D Fourier transform of the simulated systems (Figure 4 (g) and (j)) shows that the symmetry of crystal ordering is the same for experimental and simulated systems. The largest deviation occurs at small q-values, which correspond to large spatial scales. This deviation is expected, because the simulated systems are of limited size and particle number compared to the experiments.

Another difference between the experimental and simulated systems is that the simulated ellipsoidal crystal appears to have higher quality. The higher degree of crystallinity of the model may arise from the differences in electrostatic fields surrounding an experimental particle as it rotates in a field and the interaction model based on discrete charge used here. Snapshots of

simulated systems as they assemble show that a lower quality polycrystalline solid is formed first, and a slower annealing process follows (cf. Supplementary Information Figure S4). This annealing might be arrested by other factors in the experimental case.

Detailed particle position data were collected for 20 simulated seconds after the field was switched on to observe the kinetics of assembly. After 11 simulated minutes of field-assisted assembly, the field was switched off and detailed system data were again collected to observe crystal melting. Figure 5 (a) and (b) show the growth curves of projected peak area for simulation of spheres and ellipsoids. Peak areas were computed by angle-binning the Fourier domain scattering pattern of the simulated system via the same method as for the experimental SALS data (c.f. Methods). Spheres form end-to-end chains aligned with the field direction. Ellipsoids instead form zig-zag chains aligned with the field direction.[38] Both findings agree with the experiments. Despite spherical particle symmetry, Figure 5 (a) shows that peaks aligned with the field direction (peaks 2 and 5) have different kinetics relative to the other peaks. As discussed earlier, the symmetry of the peaks is broken by the anisotropic forces present due to the applied field.

Figure 5 (c) and (d) shows the same data as Figure 5 (a) and (b), but now for melting, when the simulated field is switched off. Figure 5 (c) shows that the melting kinetics of the peaks for spheres collapses onto the same curve after the field is turned off, consistent with the peak differences being a consequence of the applied electrostatic forces. Figure 5(d) reveals that unlike assembly, melting kinetics is strongly affected by the anisotropy of the particles.

In order to capture the time scale of a transition from one peak area to another, the curves were fit with the logistic decay equation:

$$A(t) = \frac{B - C}{1 + e^{-k(t - t_0)}} + C \quad (1)$$

where A(t) is the peak area of light diffraction response, B is the initial peak area value, C is the long-time value of A(t), and k is the rate constant. The larger the value of k, the faster the self-assembled structures respond to the change of the field.

Table 1 reports the assembly time constant (k) of the logistic growth function (eqn. 1) for ellipsoids and spheres relative to the assembly rate constant measured from peaks 2 and 5 of spheres, as reported in Figure 5 (a), (b). The results show that ellipsoids and spheres assemble into a crystal with long-range ordering, as quantified by the diffraction peak area, with roughly equivalent kinetics to within the uncertainty of the fitting parameters. Our results show that shape anisotropy strongly affects the melting kinetics, but not the assembly kinetics. In the field-on condition, rotation of the ellipsoidal particles is restricted by polarization-induced effects. Therefore, the rotational degrees of freedom do not significantly influence the kinetics of concentrating ellipsoids into a dense structure; the difference in the assembly rate between spheres and ellipsoids is therefore small. The assembly kinetics for crystallization are thus controlled by the strength of electrostatic forces and the translational diffusion of particles, which are seemingly similar for spheres and ellipsoids.

Table 2 reports the melting time constant (k) for ellipsoids and spheres relative to the melting rate constant measured from peaks 2 and 5 of spheres, as reported from Figure 5 (c) and (d). For spherical particles, melting occurs somewhat slower (smaller time constant) than assembly. For ellipsoidal particles, melting is ~2.4 times faster (larger time constant) than assembly. In addition, Table 2 indicates that the ellipsoids melt at a rate that is ~5.7 times faster than spheres. This dichotomous effect of anisotropy on kinetics is a key finding of the study; colloidal shape affects melting kinetics to a much greater degree than assembly kinetics.

3.4 Effect of Rotational Degrees of Freedom on Melting Rate

To understand the origin of the kinetic differences for sphere and ellipsoid melting, we investigated the effects of rotational degrees of freedom. A simulation of the melting process without particle rotation for ellipsoids was carried out. The starting configuration for this simulation was the crystal assembled under full consideration of the rotational degrees of freedom, as reported, for example, in Figure 5. Beginning at the point when the simulated field is turned off, this new simulation was carried out with the ellipsoidal particles unable to rotate. Particles in the previous simulations had 5 degrees of freedom (3 positional and 2 rotational). When rotation is not permitted only the 3 positional degrees of freedom remain.

Figure 6 shows the change in simulated SALS peak area with time of ellipsoidal particles for $N_{DOF=5}$ and $N_{DOF=3}$. When rotation is not allowed, the rate of peak area change is significantly reduced. Table 3 shows the value of the logistic fit parameter (k) for the simulations shown in Figure 6, as well as for spheres. Ellipsoids without rotational degrees of freedom are shown to melt at a very similar rate to simulated spheres. The comparison clearly indicates that the rotational degrees of freedom for these systems are responsible for the striking change in melting kinetics for spheres and ellipsoids.

During melting, the decreasing area of the light scattering peaks is a consequence of the reduced global crystal quality and the increased defect density. These defects, which lead to melting, are generated as ellipsoids undergo both translational and rotational Brownian diffusion. Of course, the rotational Brownian motion of spherical colloids does not affect their crystal ordering. That is, spherical colloids melt only by translational diffusion while both translational and rotational diffusion contribute to colloidal crystal melting of ellipsoids.

On the other hand, for assembly, the diffusion of the spheres and ellipsoids is the same as in melting; however, there exists an additional field-induced interaction that aligns and assembles particles into a dense crystal. As a result, the differences due to rotational Brownian diffusion during assembly are less dominant than for melting.

4. Discussion

4.1 The Effects of Applied Electric Field Strength and Frequency on Crystal Quality

From both SALS and CLSM data, we observed higher crystallinity of colloidal assemblies at electric field strengths greater than 24 kV/m. Singh *et al*.[38] investigated the applied electric field strengths ranging from 0 to 40 kV/m and frequencies varying between 1 and 10 kHz for 2D ellipsoids assembled by an AC electric field. As the field strength increases over 10kV/m, the induced polarization of the particles led to interparticle chaining in the field direction. Azari *et al*.[43] likewise reported a transition from fluid to either a crystal or tubular structure for electric field strengths greater than 75 kV/m, depending on the particle aspect ratio. At the applied frequency of 5 MHz, increased electric field strength leads to an increased crystallinity because of the larger strength of electrostatic coupling and induced polarization of the particles.

Turning to the effect of frequency, higher crystal quality was observed for applied frequencies greater than 0.5 MHz. The applied frequency affects self-assembly through its role in determining the polarization of the dielectric particles. That is, the polarization is affected by the movement of ions around the particles and the dielectric relaxation of the electrolyte.[44] Both of these polarization phenomena are frequency dependent. For micrometer-sized particles, ion migration around the particles is significant for kilohertz frequencies and lower. For particles in salt solution with concentrations at 0.1mM, the frequency scale for electrolyte relaxation is megahertz and lower. In our system, for a fixed electric field strength (E=32kV/m), assembly quality tended to increase as frequency was increased (Figure 2(d)). Previous studies on polarization-induced pair forces between particles[44] indicate that polarizability, and hence dipolar attraction strength, tend to decrease with frequency, because polarization mechanisms active only at slow timescales can no longer contribute to total particle polarizability. Other studies[25] have also observed complex effects of AC field frequency on ellipsoidal self-assembly; these effects warrant further study.

The order-to-disorder transition of particles under and AC electric field occurs as dipolar interaction energy scales approach and exceed the thermal energy scale.[44] However, the quality of crystalline assembly for dipolar energy scales significantly above the system thermal energy are expected to be low; for attractions which far exceed system thermal energy the number of kinetically trapped defect states is expected to be high. ‘Jammed’ states with high disorder and low

particle mobility have been observed in many attractive colloidal systems, and generally arise when interparticle attraction far exceeds thermal energy scales in dense systems.[45]

Our results indicate that higher particle polarizability does not necessarily result in a greater degree of crystalline order in dense systems. The peak voltage (which increases polarizability) and frequency (which decreases polarizability) of the applied AC field should be tuned so as not to produce jammed states. In simulation, we assume static charges on both ends of particles to represent the AC polarization modeling at higher applied frequency, similar to as reported in Azari *et al*.[43] We also maintain a fixed maximum dipolar interaction strength between particles, so as to focus on the effect of geometry alone on crystal assembly quality.

4.2 Comparison of Simulation and Experiment

The experiments and simulations, while matching qualitatively, show some quantitative differences. One difference is the magnitude of the kinetic effects observed in the ellipsoids upon melting: the melting rate constant for ellipsoids relative to spheres is greater for the experiments than the simulations (Table 2). The pair potential model employed in the simulations is a simplified representation of the true interactions; the model neglects two effects which could contribute to the discrepancy between experiments and simulations. First, bulk flows of solvent which would drive cooperative motion were not included in this MD integration method. Differences in particle shape and starting crystal structure may lead to differences in the hydrodynamics of these systems. Secondly, the discrete-charge model used here to represent particle polarization (see Supplementary Information) does not depend upon the angle of the particle relative to the applied field. Experimentally, the polarization of an ellipsoid will change depending upon its orientation relative to the field.

Another difference between experiment and simulation is the difference in melting rates observed for the two sets of diffraction peaks in the sphere systems. Despite their inherent symmetry, spherical particles are driven to assemble by the application of a unidirectional field, which breaks the symmetry of the SALS peaks aligned with that field direction. Simulation results show that crystalline order corresponding to these in-line peaks melt slower than the others, while the reverse is true of experiments (Table 2). The sphere structure can be thought of as a set of linear chains

that have joined in the direction lateral to the field via inter-chain attraction. The difference between intra- and inter-chain attractive strength controls the steady state field-on configuration of intra- and inter-chain spacing, and hence the melting kinetics of these neighbor bonds. The slower breakup of intra-chain bonds in the simulated systems implies that the discrete-charge model (see Supplementary Information) used to represent particle polarization produces a higher ratio of in-chain/out-of-chain bond strength than observed in experiment.

5. Conclusions

We have shown that crystals of ellipsoids assembled under AC fields lose their positional order during melting at rates that are more than five time more rapid than for spheres in the same condition. Molecular dynamics simulations confirm that the anisotropy of the ellipsoids has a significant effect on crystal melting kinetics, while exerting limited influence over crystal freezing kinetics. In addition, simulations of ellipsoids with and without rotational degrees of freedom demonstrate that it is the Brownian rotation of the ellipsoids that is responsible for the faster melting kinetics relative to spheres. Insights from our work can be applied to design the kinetics of reconfiguration of colloidal crystals.

6. Acknowledgement

This work was supported by the Department of Energy, Basic Energy Sciences under grant DE-SC0013562 as well as by a Rackham Graduate Student Research Grant from the University of Michigan. This research utilized computational resources and services supported by Advanced Research Computing at the University of Michigan, Ann Arbor.

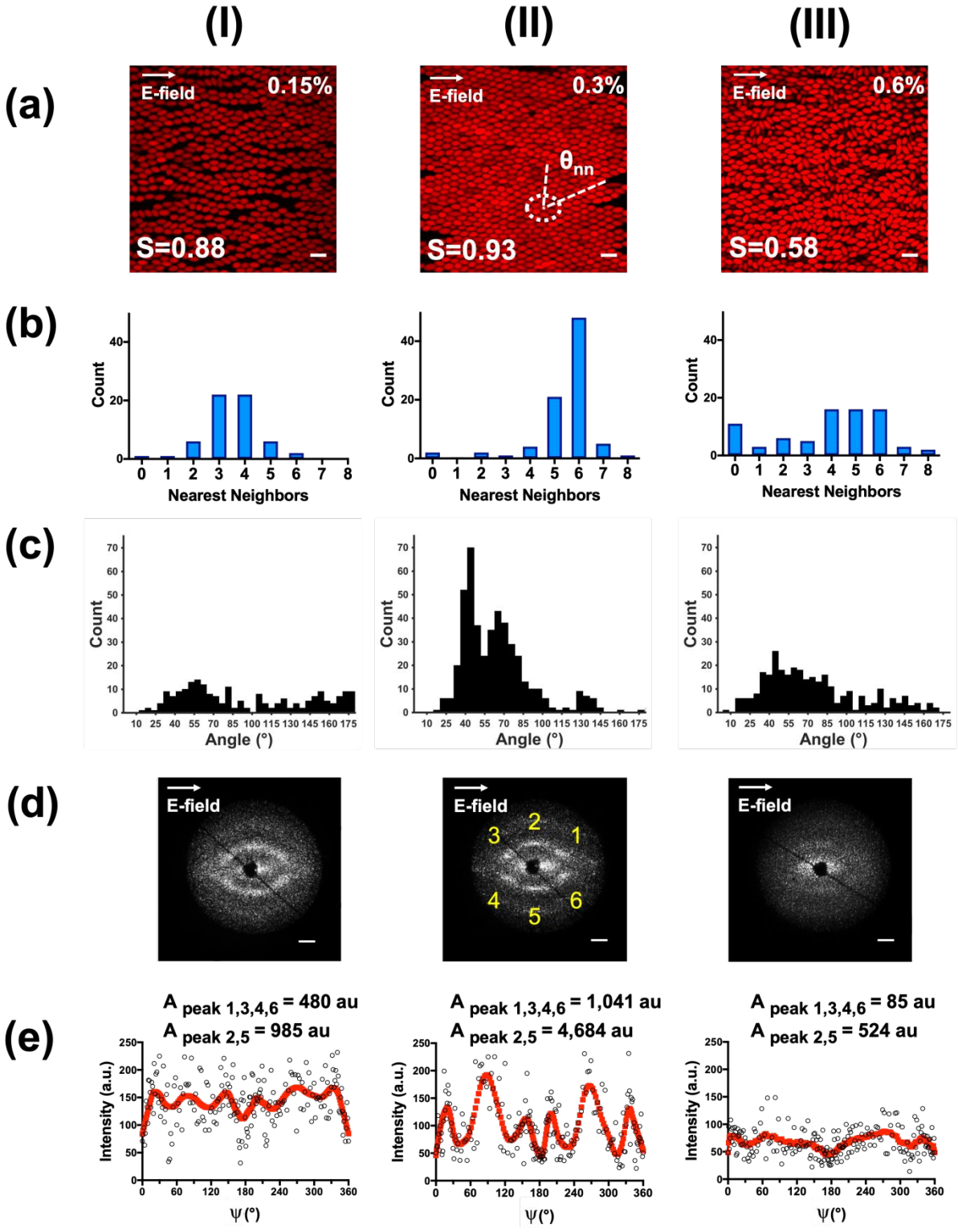

Figure 1. 2D confocal laser scanning micrographs of (a-I) a high orientational order chain-like phase, (a-II) a high positional and orientational order close-packed phase, and (a-III) a dense

positionally ordered phase. The counts of nearest neighbors of (b-I) chain-like phase, (b-II) close-packed phase, and (b-III) dense positionally ordered phase. The distribution of nearest neighboring angles of (c-I) chain-like phase, (c-II) close-packed phase, and (c-III) dense positionally ordered phase. SALS images of (d-I) chain-like phase, (d-II) close-packed phase (with peak numbering), and (d-III) dense positionally ordered phase. The intensity of light scattering responses along the azimuthal angle ψ was acquired from SALS analysis for (e-I) chains-like phase, (e-II) close-packed phase, and (e-III) dense positionally disordered phase. The black circles are SALS data points and the red-square curves are the corresponding Gaussian fitted curves. Scale bars in CLSM images are 10 μm. Scale bars in SALS images are $q = 1\mu m^{-1}$.

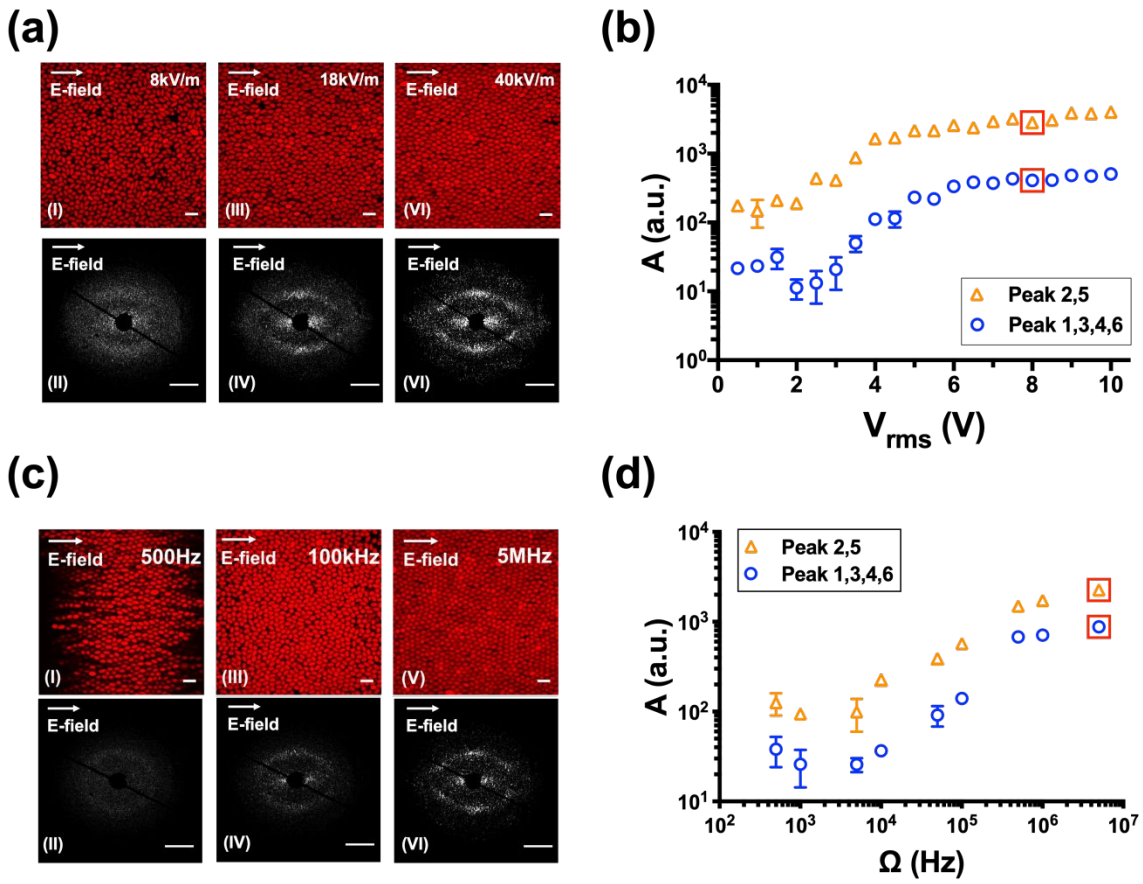

Figure 2. The impact of electric field-applied voltage and frequency on colloidal crystal quality, as quantified by peak area. (a) The CLSM and corresponding SALS images of ellipsoidal colloids assemblies under applied electric field strength at 8kV/m, 18kV/m and 40kV/m respectively. (b) The change of peak area of light diffraction response (A) under different applied electric field strength. (c) Characteristic CLSM and corresponding SALS images of ellipsoidal colloids assembled under applied frequency at 500 Hz, 100 kHz and 5 MHz, respectively. (d) The change of peak area of light diffraction response (A) under different applied frequency Ω. Scale bars in CLSM images are 10 μm. Scale bars in SALS images are $q = 1\mu m^{-1}$. E = 32 kV/m and Ω = 5MHz, shown as red boxed data points in (b) and (d), are selected field strength and frequency for further kinetic studies to ensure that the colloids assemble into high quality crystals.

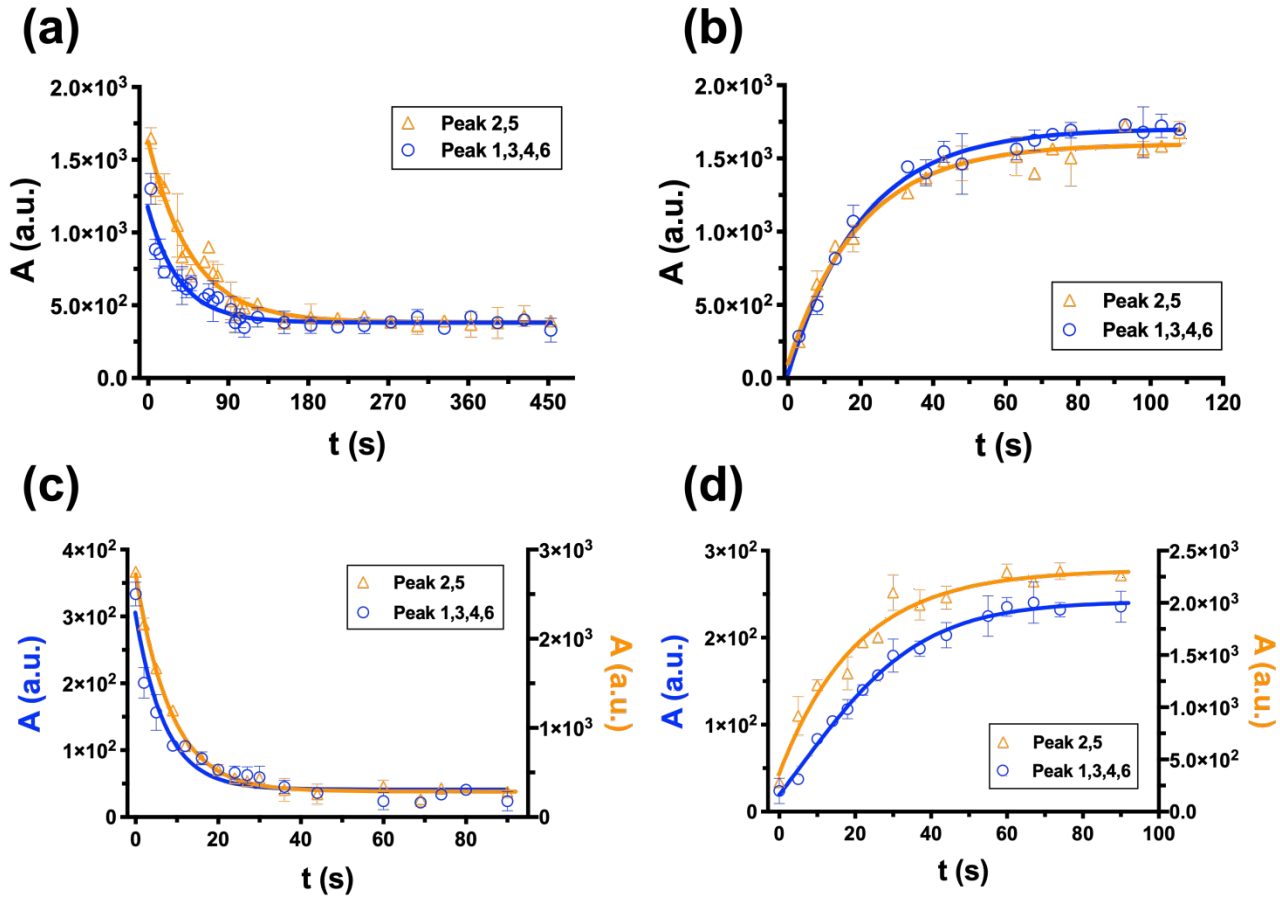

Figure 3. The change of peak area of light diffraction responses as a function of time t for (a) spherical colloid melting, (b) spherical colloid assembly, (c) ellipsoidal colloid melting, and (d) ellipsoidal colloid assembly.

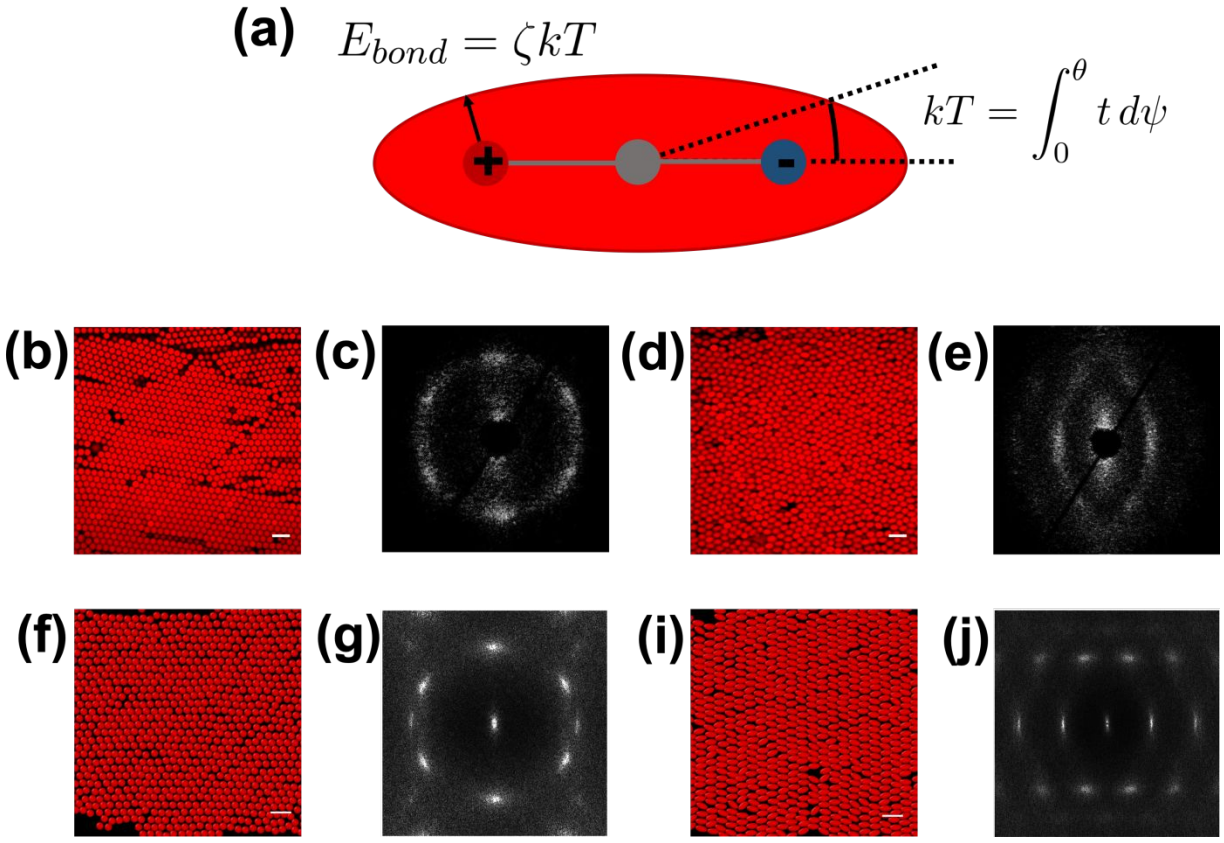

Figure 4. (a) Schematic of the interaction model used to simulate polarized particle interactions using rigid bodies and discrete charges. Experimental images of spheres (b) and ellipsoids (d) assembled into dense crystals. Matching SALS patterns for experimental sphere (c) and ellipsoid (e) systems. Images of simulated spheres (f) and ellipsoids (i) assembled into dense crystals. Matching 2D Fourier transforms of simulated spheres (g) and ellipsoids (j). Scale bars in images are 10 μm.

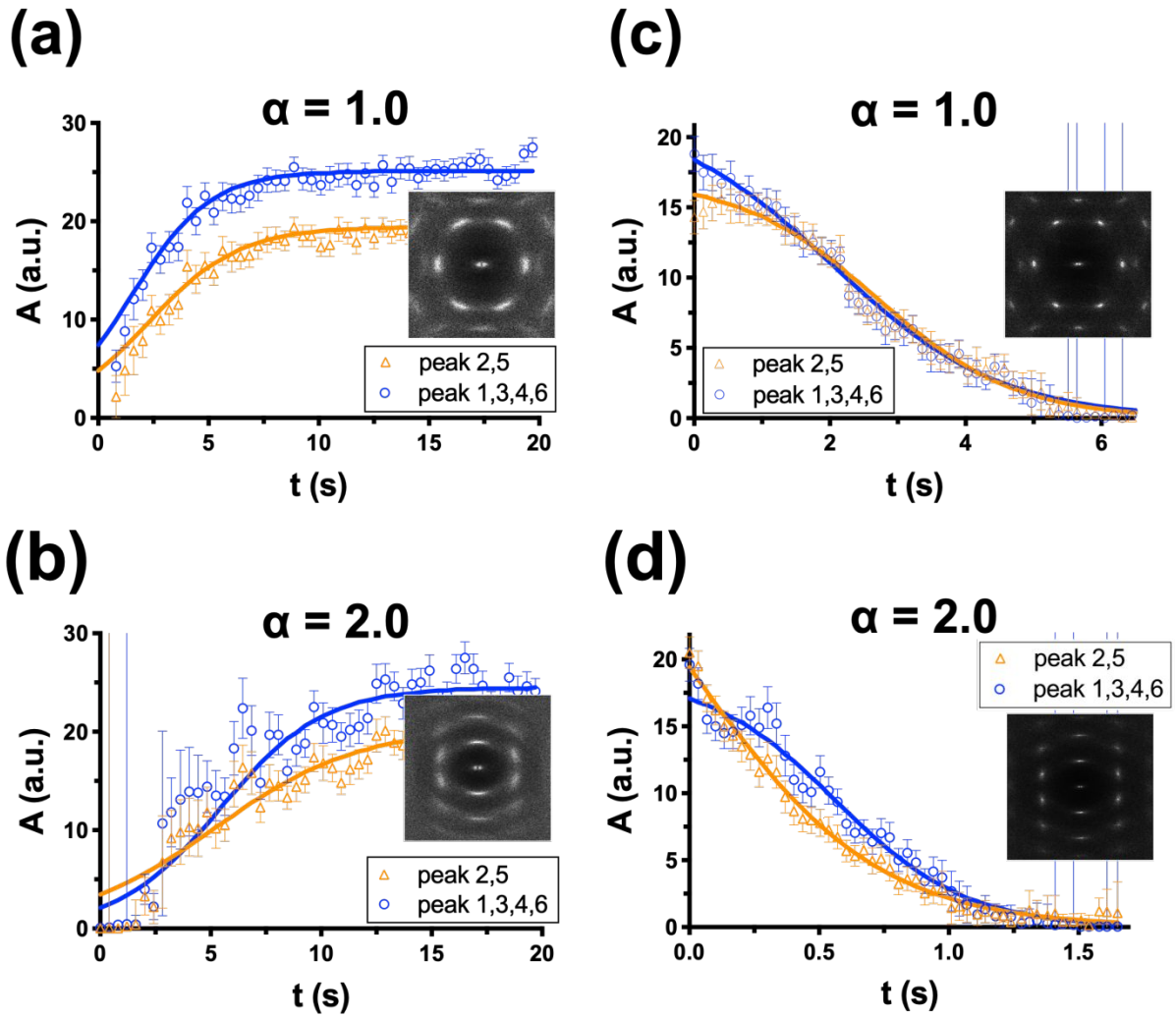

Figure 5. (a) and (b) show assembly kinetics. Projected peak area growth curves for simulated (a) spheres and (b) ellipsoids. Insets show the 2D Fourier transform of the assembled crystal structure. Error bars represent uncertainty in the peak fitting procedure. (c) and (d) show melting kinetics. Projected peak area decay curves for simulated (c) spheres and (d) ellipsoids. Insets in (c) and (d) show the Fourier transform of the crystal structure before disassembly.

Table 1 Experimental and simulated assembly rate constants for ellipsoids and spheres relative to the assembly rate constant measured from peaks 2 and 5 of spheres. Error in rate constants is found from uncertainty in fitting Eqn. 1 to experimental/simulated data

	Assembly	**Experiments**	**Simulations**
Spheres	k/k_1 (peak 2,5)	1.00 ± 0.01	1.00 ± 0.19
	k/k_1 (peak 1,3,4,6)	0.98 ± 0.01	1.16 ± 0.25
Ellipsoids	k/k_1 (peak 2,5)	0.98 ± 0.17	0.63 ± 0.19
	k/k_1 (peak 1,3,4,6)	1.21 ± 0.38	0.89 ± 0.23

Table 2 Experimental and simulated disassembly rate constants for ellipsoids and spheres relative to the disassembly rate constant measured from peaks 2 and 5 of spheres

	Melting	**Experiments**	**Simulations**
Spheres	k/k_1 (peak 2,5)	1.00 ± 0.07	1.00 ± 0.12
	k/k_1 (peak 1,3,4,6)	1.36 ± 0.09	0.83 ± 0.08
Ellipsoids	k/k_1 (peak 2,5)	5.74 ± 0.17	2.94 ± 0.32
	k/k_1 (peak 1,3,4,6)	6.76 ± 0.56	4.09 ± 0.54

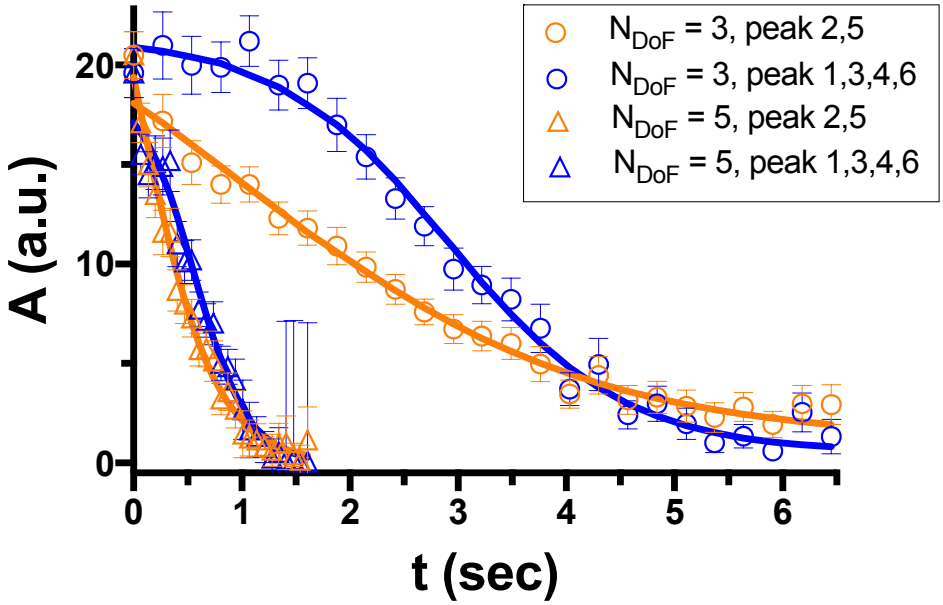

Figure 6. Change in area of the simulated SALS peaks as a function of time for a simulation of ellipsoids. Two cases are shown: melting under full translational and rotational diffusion (N_{DoF} = 5, circles) and when rotational degrees of freedom are not included (N_{DoF} = 3, triangles). Error bars are calculated from uncertainty in peak fitting, which is higher in the fluid phase.

Table 3 Simulated disassembly rate constants relative to the disassembly rate constant measured from peaks 2 and 5 of spheres at different aspect ratios with (N_{DoF} =5) or without (N_{DoF} =3) degrees of rotational freedom

		Degrees of freedom = 3	**Degrees of freedom = 5**
Spheres	k/k_1 (peak 2,5)	1.00 ± 0.12	
	k/k_1 (peak 1,3,4,6)	0.83 ± 0.08	
Ellipsoids	k/k_1 (peak 2,5)	0.64 ± 0.09	2.94 ± 0.32
	k/k_1 (peak 1,3,4,6)	1.26 ± 0.10	4.09 ± 0.54

References

1 M. J. Solomon, *Langmuir*, 2018, **34**, 11205–11219.
2 Y. Kim, A. A. Shah and M. J. Solomon, *Nat. Commun.*, 2014, **5**, 3676.
3 J. A. Ferrar and M. J. Solomon, *Soft Matter*, 2015, **11**, 3599–3611.
4 B. Liu, T. H. Besseling, M. Hermes, A. F. Demirörs, A. Imhof and A. van Blaaderen, *Nat. Commun.*, 2014, **5**, 3092.
5 A. C. Stelson, S. J. Penterman and C. M. Liddell Watson, *J. Mater. Chem. C*, 2018, **6**, 11118–11127.
6 A. C. Stelson, S. J. Penterman and C. M. Liddell Watson, *Small*, 2017, **13**, 1603509.
7 S. J. Boehm, L. Lin, K. Guzmán Betancourt, R. Emery, J. S. Mayer, T. S. Mayer and C. D. Keating, *Langmuir*, 2015, **31**, 5779–5786.
8 S. J. Boehm, L. Lin, N. Brljak, N. R. Famularo, T. S. Mayer and C. D. Keating, *Langmuir*, 2017, **33**, 10898–10906.
9 M. Caleap and B. W. Drinkwater, *Proc. Natl. Acad. Sci.*, 2014, **111**, 6226–6230.
10 A. A. Shah, M. Ganesan, J. Jocz and M. J. Solomon, *ACS Nano*, 2014, **8**, 8095–8103.
11 A. A. Shah, B. Schultz, W. Zhang, S. C. Glotzer and M. J. Solomon, *Nat. Mater.*, 2015, **14**, 117–124.
12 K. A. Willets and R. P. Van Duyne, *Annu. Rev. Phys. Chem.*, 2007, **58**, 267–297.
13 J. Teyssier, S. V. Saenko, D. van der Marel and M. C. Milinkovitch, *Nat. Commun.*, 2015, 1–7.
14 L. M. Mäthger, E. J. Denton, N. J. Marshall and R. T. Hanlon, *J. R. Soc. Interface*, 2009, **6**, S149–S163.
15 S. Kinoshita, S. Yoshioka and J. Miyazaki, *Reports Prog. Phys.*, 2008, **71**, 076401.
16 R. E. Rodríguez, S. P. Agarwal, S. An, E. Kazyak, D. Das, W. Shang, R. Skye, T. Deng and N. P. Dasgupta, *ACS Appl. Mater. Interfaces*, 2018, **10**, 4614–4621.
17 A. D. Pris, Y. Utturkar, C. Surman, W. G. Morris, A. Vert, S. Zalyubovskiy, T. Deng, H. T. Ghiradella and R. A. Potyrailo, *Nat. Photonics*, 2012, **6**, 195–200.
18 J. M. Weissman, H. B. Sunkara, A. S. Tse and S. A. Asher, *Science*, 1996, **274**, 959–963.
19 S. H. Kim, J. G. Park, T. M. Choi, V. N. Manoharan and D. A. Weitz, *Nat. Commun.*, 2014, **5**, 1–8.
20 T. S. Shim, S. H. Kim, J. Y. Sim, J. M. Lim and S. M. Yang, *Adv. Mater.*, 2010, **22**, 4494–4498.
21 H. Hwang, D. A. Weitz and F. Spaepen, *Proc. Natl. Acad. Sci.*, 2019, **116**, 1180–1184.
22 Y. L. Wu, D. Derks, A. van Blaaderen and A. Imhof, *Proc. Natl. Acad. Sci.*, 2009, **106**, 10564–10569.
23 T. Palberg, *J. Phys. Condens. Matter*, 2014, **26**, 333101.
24 S. C. Glotzer and M. J. Solomon, *Nat. Mater.*, 2007, **6**, 557–562.
25 J. J. Crassous, A. M. Mihut, E. Wernersson, P. Pfleiderer, J. Vermant, P. Linse and P. Schurtenberger, *Nat. Commun.*, 2014, **5**, 5516.
26 F. Ferri, *Rev. Sci. Instrum.*, 1997, **68**, 2265–2274.
27 J. K. G. Dhont, C. Smits and H. N. W. Lekkerkerker, *J. Colloid Interface Sci.*, 1992, **152**, 386–401.
28 A. A. Shah, H. Kang, K. L. Kohlstedt, K. H. Ahn, S. C. Glotzer, C. W. Monroe and M. J. Solomon, *Small*, 2012, **8**, 1551–1562.
29 S. V. Savenko and M. Dijkstra, *Phys. Rev. E*, 2004, **70**, 051401.

30 A. Mohraz and M. J. Solomon, *Langmuir*, 2005, **21**, 5298–5306.
31 D. Andrienko, *J. Mol. Liq.*, 2018, **267**, 520–541.
32 D. K. Cinader and W. R. Burghardt, *Macromolecules*, 1998, **31**, 9099–9102.
33 M. Ganesan and M. J. Solomon, *Soft Matter*, 2017, **13**, 3768–3776.
34 A. Somwangthanaroj, E. C. Lee and M. J. Solomon, *Macromolecules*, 2003, **36**, 2333–2342.
35 W. S. Cleveland, *J. Am. Stat. Assoc.*, 1979, **74**, 829–836.
36 J. A. Anderson, C. D. Lorenz and A. Travesset, *J. Comput. Phys.*, 2008, **227**, 5342–5359.
37 T. D. Nguyen, C. L. Phillips, J. A. Anderson and S. C. Glotzer, *Comput. Phys. Commun.*, 2011, **182**, 2307–2313.
38 J. P. Singh, P. P. Lele, F. Nettesheim, N. J. Wagner and E. M. Furst, *Phys. Rev. E*, 2009, **79**, 050401.
39 G. Yatsenko and K. S. Schweizer, *Langmuir*, 2008, **24**, 7474–7484.
40 D. Mukhija and M. J. Solomon, *Soft Matter*, 2011, **7**, 540–545.
41 P. Mazeron and S. Muller, *Appl. Opt.*, 1996, **35**, 3726–3735.
42 A. Ramos, H. Morgan, N. G. Green and A. Castellanos, *J. Colloid Interface Sci.*, 1999, **217**, 420–422.
43 A. Azari, J. J. Crassous, A. M. Mihut, E. Bialik, P. Schurtenberger, J. Stenhammar and P. Linse, *Langmuir*, 2017, **33**, 13834–13840.
44 M. Mittal, P. P. Lele, E. W. Kaler and E. M. Furst, *J. Chem. Phys.*, 2008, **129**, 064513.
45 V. Trappe, V. Prasad, L. Cipelletti, P. N. Segre and D. A. Weitz, *Nature*, 2001, **411**, 772–775.

Table of Contents Entry

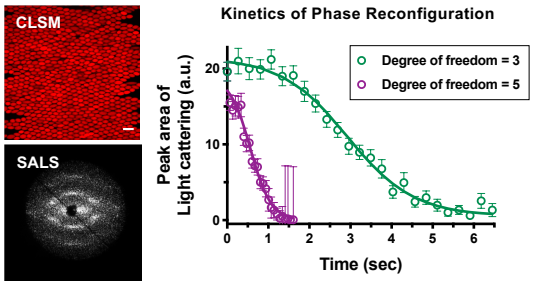

Effects of shape anisotropy on colloids reconfiguration kinetics: crystals of ellipsoids melt at rates 5.7 times faster than spheres.